Vacuum 212 (2023) 112041

Contents lists available at ScienceDirect

Vacuum

journal homepage: www.elsevier.com/locate/vacuum

HiPIMS deposition of superconducting Nb thin films onto Cu substrates

S. Leith [a,1], J. Qiao [a], M. Vogel [a,*], E. Seiler [b], R. Ries [b], Y. Li [c], C. Wiktor [c], J. Mueller [c], Y. Sakalli [c,d], B. Butz [c], X. Jiang [a,**]

[a] Chair of Surface and Materials Technology, University of Siegen, Siegen, Germany
[b] Institute of Electrical Engineering SAS, Bratislava, Slovakia
[c] Micro- and Nanoanalytics Group, University of Siegen, Siegen, Germany
[d] Micro- and Nanoanalytics Facility, University of Siegen, Siegen, Germany

ARTICLE INFO

Keywords:
SRF cavity
HiPIMS
Nb thin film
Nb/Cu
First magnetic flux entry field

ABSTRACT

The use of energetic condensation techniques, such as HiPIMS, has the potential to significantly improve the superconducting performance of coated Cu cavities by producing bulk-like Nb thin films. However, in order to benefit from these techniques, a deeper understanding of the effects of, and the relationship between, the different deposition parameters, the physical properties of the deposited films and the superconducting performance of the films, is still required. This contribution details the effects of different HiPIMS deposition parameters on the morphological, crystallographic and superconducting properties of Nb thin films deposited onto electropolished Cu substrates. Higher duty cycles (8 – 20 %) than previous HiPIMS investigations were used in the majority of the coatings. The films displayed more bulk-like crystallographic properties, indicated here by the lattice parameter, with a "transition zone" apparent in the early stages of film growth. A reduction in the surface roughness as well as interfacial voids, compared to typical DC MS Nb films, was also observed. The superconducting performance of the films, specifically the first magnetic flux entry field, showed a marked reliance on the substrate bias and the film thickness. Conversely, the HiPIMS duty cycle appears to have a comparatively insignificant effect.

1. Introduction

Thin film coated cavities, typically composed of a Nb thin film deposited onto a Cu cavity, have been used successfully in particle accelerators for a number of years already, most notably at CERN for the LEP-II and LHC accelerators [1,2]. However, these cavities are typically limited to low field operation, due to the so-called "Q-slope", which describes the significant reduction in quality factor, at fields above 15 MV/m, observed in these cavities [3]. An extensive amount of research has already been conducted in order to overcome the Q-slope issue. However, no single specific origin has been identified [4–6].

With the ever increasing performance requirements of future accelerators, in combination with the potential cost savings offered by Nb coated thin film cavities, there is still great incentive to improve their performance. Furthermore, the deposition of Superconductor-Insulator-Superconductor (SIS) film structures on Cu cavities requires a smooth, homogeneous and bulk-like Nb base layer for effective use [7].

In this regard, various methods are currently being pursued, with a focus on energetic condensation techniques. These techniques typically utilise metallic ions of Nb, which allow for greater control of the growing film during deposition [8,9]. This is particularly relevant for Cu cavities, which cannot be heated to the high temperatures associated with enhanced surface diffusion. Significant improvements to the thin film microstructure, density, adhesion and superconducting performance of Nb have already been documented through the use of some of these techniques. These include: Electron Cyclotron Resonance (ECR) [10], Ultra High Vacuum Cathodic Arc (UHVCA) [11,12], Coaxial Energetic Deposition (CED) [13] and High Power Impulse Magnetron Sputtering (HiPIMS) [14–17]. Due to its ease of adaptability to already existing cavity coating systems, HiPIMS is of leading interest.

The relationship between the substrate and the resultant Nb film has also been extensively studied due to the known effects of the Nb

* Corresponding author.
** Corresponding author.
E-mail addresses: Michael.Vogel@uni-siegen.de (M. Vogel), Xin.Jiang@uni-siegen.de (X. Jiang).
[1] Present Address: CERN, European Organization for Nuclear Research 1211 Geneva 23, Switzerland.

https://doi.org/10.1016/j.vacuum.2023.112041
Received 28 August 2022; Received in revised form 19 November 2022; Accepted 23 March 2023
Available online 24 March 2023

topography and microstructure on superconducting performance [18,19]. Deposition on oxidised Cu leads to smaller grains and a Nb (110) texture [20]. ECR Nb deposition on Cu single crystals resulted in specific Nb/Cu orientation relationships, while similar coatings on polycrystalline Cu showed a higher degree of anisotropy in the film [21]. Similar results were obtained for both CED™ and HiPIMS deposition on polycrystalline Cu substrates, which exhibited polycrystalline Nb films with a Nb (110) preference [13,22].

This study focused on investigating the effects of changing deposition parameters on the microstructural, crystallographic and superconducting properties of Nb thin films deposited onto polycrystalline Cu substrates via HiPIMS. The study was focused on relatively low temperature coatings, aimed at maintaining the structural integrity of the Cu cavities, with high temperature coatings having been previously studied [23].

2. Experimental

The Nb thin films described in this study were deposited using HiPIMS with a fixed target to substrate distance of 55 mm. The films were deposited using a 100 × 88 mm^2 Nb target (RRR 300) and Ar gas (99.999 Vol-%) in a commercial, high-volume, fully automated coating system (CemeCon CC800). HiPIMS operation was achieved using an ADL DC power supply coupled to a capacitor storage scheme controlled by a programmable operating system. A further dedicated ADL DC power supply was also used for the substrate biasing.

The substrates used were 1 mm thick, polycrystalline, OFE (Oxygen-Free Electronic) Cu samples with dimensions of 25 × 25 mm^2, as well as pieces of Si (100) wafer, which were used as reference samples. The Cu samples were prepared with mechanical polishing, followed by electropolishing in a solution of phosphoric acid (85 %) (H_3PO_4) and n-butanol ($C_4H_{10}O$) in a 3:2 ratio. This led to a typical Root-Mean-Square (RMS) surface roughness of $S_q = 3.6 \pm 1.5$ nm of the used Cu substrates, based on multiple 20 × 20 μm^2 Atomic Force Microscope (AFM) scans. EBSD analysis of 3 separate Cu samples following electropolishing showed an average Cu grain diameter of 4.1 ± 4.3 μm.

Prior to deposition, the system, including the substrates, was baked at 290 °C for 6 h. The system was then allowed to cool to the coating temperature, typically 180 °C for this work, where a base pressure of ~ 6.0 x 10^{-7} mbar was reached prior to coating. This was controlled by programming requirements into the coating system software. Owing to the nature of the deposition system, the substrate temperature could not be monitored during sample coating. Instead, the values reported here for the substrate temperature were acquired separately during multiple separate trials. The power setting of the resistance heater and the resultant temperature measured by a thermocouple connected to the resistance heater were correlated to the temperature measured by a thermocouple placed on the substrate holder for each power setting used during the deposition processes.

Once the coating temperature was reached the substrates were subjected to a medium frequency (MF) plasma etching process for 10 min as a final surface treatment. During this process, medium frequency RF power (650 V, 240 kHz) supplied by an Advanced Energy Pinnacle Plus unit was applied to the substrate holder in conjunction with injection of inert Ar gas into the deposition chamber. This led to the creation of Ar^+ ions, which interact with the substrate, resulting in sputter cleaning of its surface. The final step before the Nb film coating was sputter cleaning of the Nb target for 10 min.

Typical HiPIMS deposition processes use a low duty cycle value, in the region of 1 – 10 % [14,24]. However, stable plasma conditions across a range of deposition parameters, while operating at a low deposition pressure (8.0 x 10^{-3} mbar), were found to require a duty cycle > 8 %, other than for specific parameter combinations. For this reason, the bulk of the testing in this study was completed at a duty cycle of 10 %, but ranged between 2 and 20 %. All the samples were deposited using a DC substrate bias. The parameter ranges explored in this study are presented in Table 1.

Multiple series of coatings were completed in this study, with each series focused on the effects of changing only a single deposition parameter. This resulted in a specific set of "base" parameter settings for the coatings, which are displayed in Table 2. The parameters which were varied in this study include the: cathode power (P), deposition pressure (p_{dep}), HiPIMS pulse length (t_{pulse}), HiPIMS pulse frequency (f_{pulse}), substrate bias (U_B) and the substrate temperature (T_s). Unless otherwise specified, film thicknesses were maintained > 2.5 μm, in order to allow for better comparability of the superconductivity test results. As a final experiment, a series of films was deposited with equal deposition parameters, similar to those detailed in Table 2, albeit with a pulse length of 120 μs, and thickness values ranging from 0.91 to 8.10 μm. Also included in Table 2 are the deposition parameters used to deposit the reference DC MS Nb film referred to in this paper. This recipe was also used to deposit the initial QPR sample (Sample B2.4) for the ARIES collaboration program [25].

During the film deposition process, the HiPIMS pulse signals (hereafter referred to as waveforms) were collected from the cathode using a 4-channel Picoscope 2000 Series compact oscilloscope.

Microstructural analysis of the films was completed using a Zeiss Ultra 55 Scanning Electron Microscope (SEM). The surface morphology of the samples was examined with a Halcyonics XE-100 AFM in non-contact mode, with a scan size of 20 x 20 μm^2.

The film thickness measurements were completed with X-Ray Fluorescence (XRF) using an XDAL Fischerscope X-ray system. A 10 × 25 mm^2 section of each sample was measured 15 times, with equal spacing between points, in order to obtain a final average thickness value.

The crystallographic characteristics of the films were determined with X-ray diffraction (XRD) (Panalytical Empyrean diffractometer). A Cu Kα source was used to complete θ - 2θ Bragg-Brentano scans of each sample. The average crystallite sizes of all samples were calculated using the Scherrer equation while the lattice parameters were determined using the Bragg equation. The instrumental broadening was accounted for by the use of a lanthanum hexaboride standard sample. A selection of samples was also subjected to pole figure measurements for texture studies. These scans were completed using the parallel beam XRD optics and a spot size of 4 × 4 mm^2 for all measurements. During the measurements, the stage was rotated through φ = 0 – 360° in steps of 5°, with a time of 1.5 s per step. The stage was also tilted through χ = 0 – 80° in 5° steps. A background scan was collected for all pole figure measurements to decrease the level of noise in the results. The defocusing of the X-ray beam at large tilt angles (> 60°) was accounted for based on the equation developed by Gale and Griffiths [26].

For further microstructure and crystallographic analysis of the best performing HiPIMS Nb/Cu samples (in terms of their first magnetic flux entry field), a ThermoFischer FEI Talos F200X Transmission Electron Microscope (TEM) has been employed. The TEM lamellae were prepared using a dual-beam Focused Ion Beam (FIB) (ThermoFischer FEI Helios Nano Lab 600) by applying the standard lift-out technique. In this process, a lamella was first attached to a support TEM Cu-grid and subsequently thinned down to electron transparency by sequentially reducing the ion-beam energy to reduce beam damage. In addition, the dual-beam FIB system also allowed for in-depth investigations of the Nb/Cu

Table 1
HiPIMS Nb deposition parameters and range of values.

Parameter	Value
Cathode Power (P)	300 – 600 W
Deposition Pressure (p_{dep})	8 × 10^{-3} to 1.8 x 10^{-2} mbar
HiPIMS Pulse Length (t_{pulse})	80 – 200 μs
HiPIMS Pulse Frequency (f_{pulse})	200 – 2000 Hz
Duty Cycle (Calculated)	2 – 20 %
Substrate Bias (DC) (U_B)	0 to -250 V
Substrate Temperature (T_s)	115 – 290 °C
Film Thickness	0.91 – 8.10 μm

Table 2
Deposition parameters of the DC MS deposited Nb reference film and the base HiPIMS deposited Nb film.

	P_{ave} (W)	p_{dep} (mbar)	t_{pulse} (μs)	f_{pulse} (Hz)	U_B (V)	T_s (°C)
DC MS	400	8.0×10^{-3}	–	–	–	290
HiPIMS	400	8.0×10^{-3}	100	1000	−50	180

interface.

The FIB system is also fitted with an EDAX/TSL 3D Electron Backscatter Diffraction (EBSD) Pegasus - XM 4 detector for crystal structure investigations. Typical step sizes of 0.01 – 0.02 μm were used during analysis. For the EBSD surface analysis detailed in this work, no specific sample preparation process was followed as the samples were treated with EP prior to coating, and thus were already sufficiently smooth for EBSD analysis immediately after the coating. For the cross section analysis, the samples were prepared using a JEOL IB-19500CP Cross Section Polisher. Ar^+ ions of successively lower energies (8 kV, 6 kV and 4 kV) were used to achieve a smooth imageable surface.

Sections of all samples were used in DC magnetisation studies to investigate their basic superconducting properties; the critical temperature (T_c) and the first magnetic flux entry field, further denoted as the "entry field" ($\mu_0 H_{en}$). Small samples of approximately 2 × 2 mm^2 were tested using a Vibrating Sample Magnetometer (VSM) option of the commercial Physical Property Measurement System (PPMS) – Model 6000, from Quantum Design Inc. The exact measurement procedure has been described elsewhere [7].

3. Results and discussion

The results obtained in this study will be described based on the different analysis techniques involved. Any specific differences as a result of changes to the base HiPIMS deposition parameter setpoints, detailed in Table 2, will be indicated.

3.1. Waveform analysis

Waveforms were captured during the deposition of all samples in order to verify stable plasma conditions and to measure the peak current and voltage at the target. While operating at a constant 10 % duty cycle, increasing the cathode power from 300 to 600 W led to a peak current increase from 15.5 to 22.5 A, while increasing the deposition pressure from 8.0×10^{-3} to 1.8×10^{-2} mbar led to a peak current increase from 18.2 to 26.2 A. This equates to current densities in the range of 180 – 300 mA/cm^2. These values represent an approximate 20-fold increase over the typical current values measured during DC MS Nb coatings with similar settings [27].

The most apparent changes to the peak current values were as a result of adjusting the HiPIMS duty cycle, which is reliant on both the pulse length and the pulse frequency. As a result of this dual reliance, it is possible to have equal duty cycles with different combinations of the pulse length and frequency. For example, a pulse length of 120 μs and a frequency of 1000 Hz result in a duty cycle of 12 %. Similarly, a pulse length of 100 μs and a frequency of 1200 Hz also result in a duty cycle of 12 %. Two separate series of samples were deposited with equal duty cycle values, while individually changing either the pulse length or frequency, as shown in Fig. 1(a) and (b) respectively.

A roughly 2-fold increase in the peak current is observed when moving from a 20 % to an 8 % duty cycle value, as shown in Fig. 2, which likely results in increased ionisation of the sputtered material, as indicated previously [28–30]. The changes in the duty cycle, and therefore the peak current, also result in changes to the deposition rate, as depicted in Fig. 2. As the duty cycle is decreased from 20 % to 8 %, the deposition rate initially increases, up to a specific maximum, followed by a decrease with further reduction of the duty cycle. The phenomenon of decreasing deposition rate with increasing target current density is

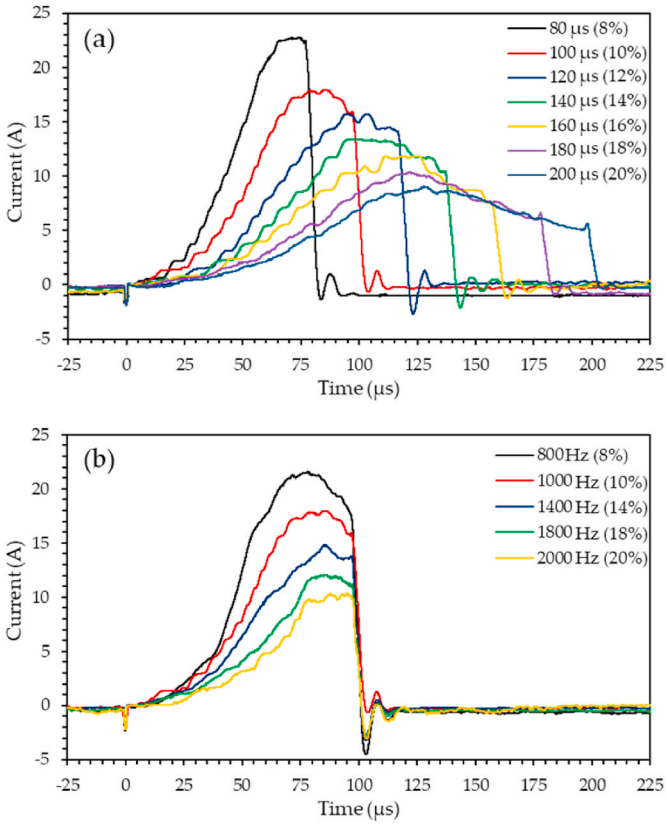

Fig. 1. Cathode current waveforms acquired during Nb deposition with HiPIMS for (a) a constant pulse frequency of 1000 Hz with different pulse length values and (b) a constant pulse length of 100 μs with different pulse frequency values. The respective duty cycles are also indicated in the legends of the figures.

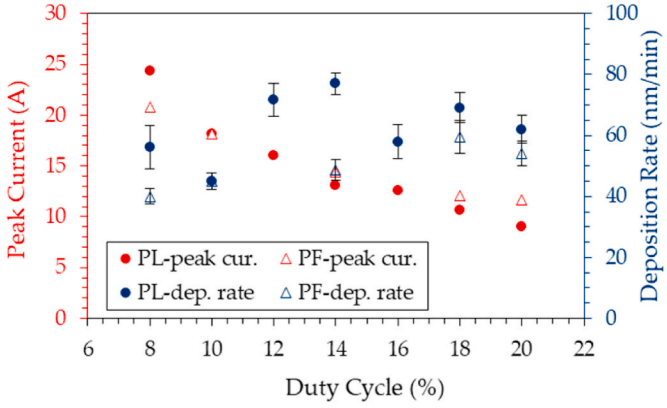

Fig. 2. Plot detailing the change in the deposition rate (blue symbols) and peak current (red symbols) as a result of changes to the duty cycle, which is dependent on the pulse length (PL) (solid circles) and pulse frequency (PF) (open triangles). Two separate series of samples were coated. Initially the pulse frequency was held constant at 1000 Hz while the pulse length was varied from 80 to 200 μs and subsequently the pulse length was held constant at 100 μs while the pulse frequency was varied from 800 to 2000 Hz.

attributed to the "return effect", i.e. back attraction of ionized target species. This has been shown for duty cycles up to 10 % [31]. In this study we found that this return effect can be extended for duty cycles up to 14 %. At such high duty cycles the metal ionisation is seemingly still high enough to show the return effect. For longer pulses or higher frequencies, i.e. higher duty cycles, the return effect is no longer prevalent. There is an obvious discrepancy between the change of duty cycle

through frequency and pulse length. This phenomenon, however, is not part of this study.

A separate series of films were deposited at different pulse lengths and frequencies to explore the low duty cycle regime (2 – 4 %). To achieve stable plasma conditions with the lower duty cycle settings, the deposition pressure was increased to 1.0×10^{-2} mbar and the cathode power decreased to 300 W average power. This resulted in an increase in the maximum current, to the highest value found in this study of ~ 56 A. Interestingly, operation at lower duty cycles led to the appearance of a smaller, secondary peak in the current waveform, as shown in Fig. 3. This peak is believed to indicate the onset of self-sputtering and has previously been documented for HiPIMS Nb operation [32]. This typically occurs near the start of high power operation following runaway. However, the lifetime of the secondary peak is short, with the current dropping likely due to gas rarefaction [33].

Due to the lower deposition rate observed at these lower duty cycles, the film thicknesses of these films ranged between 1.3 and 2.9 μm. Therefore, due to the observed reliance of the superconducting performance of the films on their thickness, detailed in Section 3.4, the comparability of these films was unsatisfactory and further results for these films are not reported here.

3.2. Topographical and microstructural analysis

With the exception of the substrate bias, changing the deposition parameters was found to have a relatively insignificant influence on the surface morphology of the Nb films as well as the individual grains themselves. As such, a typical HiPIMS Nb film surface prepared using the deposition parameters detailed in Table 2, which is representative of the majority of samples, is presented and discussed here, while any significant changes will be indicated later.

It is evident from the SEM image in Fig. 4 (a) that the Nb film surface possesses a multitude of different grain morphologies. Six distinct surface morphologies were identified and are shown in greater detail in the additional SEM images at increased magnification presented in Fig. 4 (b).

To investigate the orientation of the Nb grains in the deposited films and also a possible relationship between the surface morphology of a grain and its orientation, the area shown in the SEM image in Fig. 4 (c) was also investigated via EBSD, with the resultant Orientation Index Map (OIM) displayed in Fig. 4 (d). The EBSD results do not consistently show an individual crystallographic orientation for each grain morphology. For example, the yellow demarcated region in Fig. 4 (c), which is constituted by a grain morphology similar to (b-3), displays a variety of different orientations. This does not necessarily agree with previous research where the morphology displayed in (b-3) was

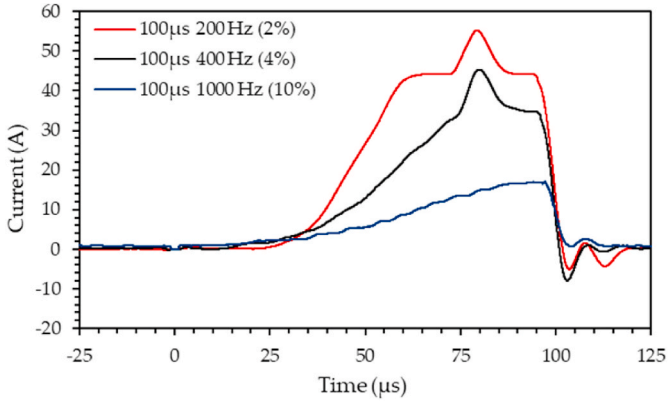

Fig. 3. Cathode current waveforms acquired during Nb deposition with low duty cycle HiPIMS completed with a 100 μs pulse length and different pulse frequency settings. The duty cycles are indicated in the brackets in the legend.

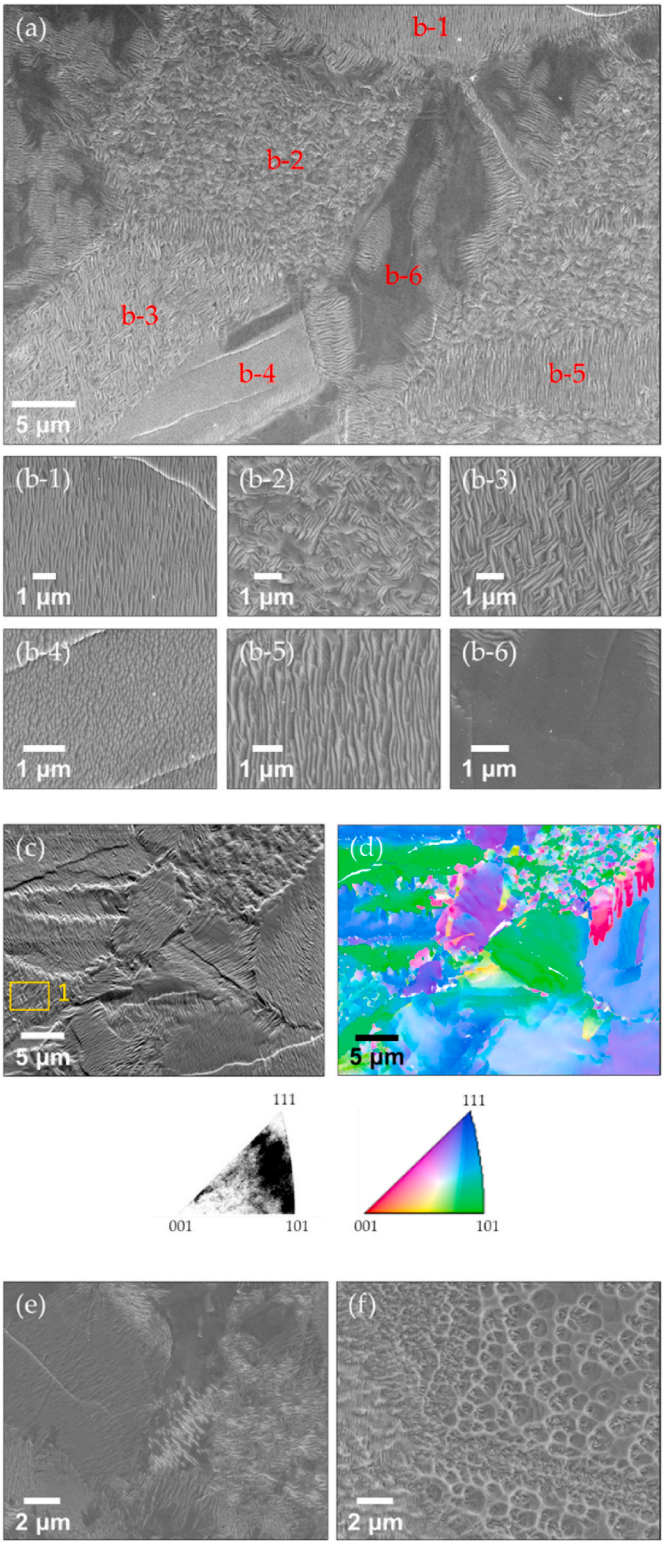

Fig. 4. Indicative surface images of the typical grain morphology observed in this study for HiPIMS Nb films deposited on Cu. (a) SEM image of multi-grain region. (b) Magnified SEM images of demarcated grain structures. (c) SEM image of EBSD-investigated multi-grain region. (d) EBSD OIM image of the same position. SEM images of (e) Nb film surface coated with 0 V DC substrate bias and (f) Nb film surface coated with -250 V DC substrate bias.

assigned to the (110) orientation [19]. However, the aforementioned study was completed on singly-oriented Cu (100) films deposited onto Si (100) substrates as opposed to the polycrystalline Cu substrates used here. Further to this, the orientation indexing of Nb grains of similar grain morphology was also inconsistent across multiple samples. Thus, it appears as if there is no correlation between the morphology of a specific Nb grain and its crystal orientation. It is therefore likely that the morphology of the Nb film surface is instead reliant on the morphology of the Cu surface onto which it is grown as opposed to the orientation of the Nb grain itself.

Due to the different grain morphologies present on the film surface, the Nb films display separate regions, each characterised by a specific range of grain sizes. As evident in Fig. 4 (d), areas with small (100's of nm) or large (μm) scale grains have been observed. However, the grain sizes do not follow a specific multimodal distribution across the samples. This was verified by further EBSD analysis of the as-deposited films, an example of which is shown in Fig. 11, as well as EBSD analysis of the film cross-section, presented in Fig. 12.

Changes to the substrate bias, which was varied between 0 and -250 V, in steps of 50 V, had the most significant impact on the Nb surface morphology. At substrate bias levels greater than -200 V, damage to the Nb film surface becomes evident. This is presented in the SEM images shown in Fig. 4(e) and (f), which compare the surfaces of the films deposited with -50 V and -250 V respectively. Instead of the homogeneous grain morphologies detailed in (e), the film surface in (f) shows evidence of surface damage as well as pitting, resulting in surface asperities due to disruptions during grain growth. This also leads to an increase in the surface roughness, detailed in Table 3. The modification of the surface is attributed to the onset of resputtering of the deposited Nb film as the impact energy of the impinging ions increases considerably above the surface binding energy of Nb [34]. In conjunction with this, the films show a continuously decreasing film thickness with increasing substrate bias. This is attributed to a combination of an increase in the film density and the resputtering of the deposited film, with resputtering dominating at higher substrate bias values.

AFM images show the surface roughness of the deposited Nb films to be dependent on the respective film surface morphology of the individual grains, as presented in Fig. 4 (b), as well as the height difference of the Cu grains in the underlying substrate, indicated in Fig. 5 (a). The Nb grain morphology affects the surface roughness on a nanometre scale while the differential height between different Cu grains acts on a scale of tens of nanometre. The surface roughness of the Nb films is therefore an average of the roughness of the different grain morphologies present in each measurement as well as the step heights between underlying Cu grains. An indicative AFM scan is presented in Fig. 5 (b), with similar features to the SEM images visible.

The apparent step height between different Cu grains, which is evident in Fig. 5 (a), occurs as a result of the differential polishing rate of individual Cu grains during the EP preparation process. These features are further present in the overgrown Nb film, as shown in Fig. 5 (b), with typical measured values of 10 – 20 nm and a maximum for all films of ~ 60 nm.

These steps resulted in a general increase in the average surface roughness compared to that measured within an individual Nb grain. Thus, for the sake of comparability, efforts were made to measure the roughness of regions of the Nb films displaying the same grain morphology on each separate sample. This provided a better idea of the changes in the surface roughness as a result of the different deposition parameters, while also removing the effects of the steps found at Cu grain boundaries in the measurements.

Table 3
Deposition parameter effect on the surface roughness (S_q) of Nb films as measured by AFM.

P (W)	p_{dep} (mbar)	t_{pulse} (μs)	f_{pulse} (Hz)	U_B (V)	T_s (°C)
+	–	none	none	+	none

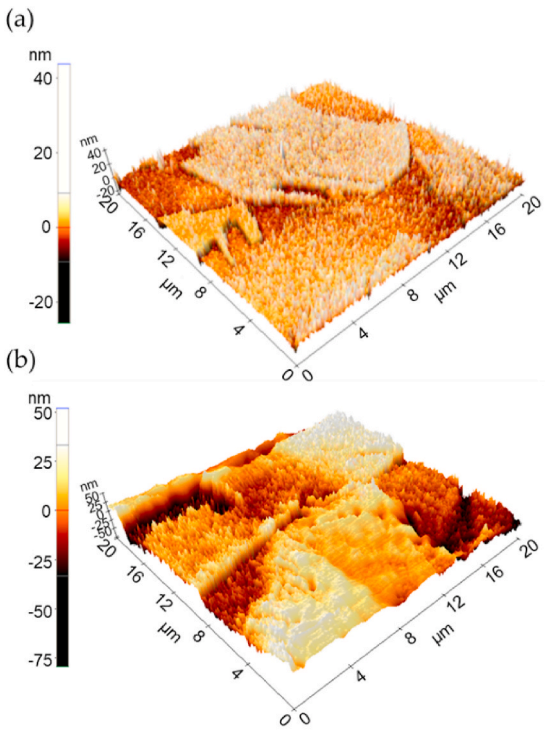

Fig. 5. Indicative AFM images of (a) a typical Cu substrate surface used in this study following the normal surface preparation procedure and (b) a representative Nb film surface from this study. The images show the local roughness variation due to both the different Cu and Nb grain morphologies as well as the effect of the step grain boundaries on the global film roughness.

The effects of increasing the individual deposition parameter values on the surface roughness are detailed in Table 3, with (+) indicating an increase in surface roughness and (−) indicating a decrease in surface roughness. The increased roughness with increasing cathode power and substrate bias corresponds to the results obtained by Burton et al. [22]. A further notable increase in the surface roughness is found when increasing the film thickness.

Overall, when comparing Nb films deposited with similar deposition parameters, as detailed in Table 2, the use of HiPIMS resulted in a decrease in the RMS surface roughness of the Nb films compared to previous DC MS deposited films, from 16.9 ± 0.9 nm (DC MS) to 11.2 ± 0.3 nm (HiPIMS), similar to previous studies [35].

The purported improvement of the Nb/Cu interface, i.e. the reduction of interfacial voids, as a result of HiPIMS deposition was also investigated. FIB cuts as well as cross-sections prepared by Ar^+ ion polishing of a series of samples were investigated via SEM to compare the presence of voids at the interface to previously studied DC MS Nb coatings, an example of which is presented in Fig. 6 (a). The areas used for this analysis typically displayed a 20 μm length of the Nb/Cu interface. Due to the time-consuming nature of these measurements, only samples coated using the upper and lower bound values of the different deposition parameters were investigated. Approximately 40 samples, 20 deposited with DC MS and 20 deposited with HiPIMS, were analysed. Three positions on each sample, randomly selected, were inspected for the presence of interfacial voids. From these results, a reduction in interfacial voids of ~ 87.5 % has been achieved through the use of HiPIMS, based on the number of positions imaged which possessed voids. All DC MS deposited films which were inspected displayed voids, with a total of 48 voids found. On the other hand, only four HiPIMS deposited films displayed voids, with a total number of six voids found for all inspected films. A comparison between a typical DC MS (a) and HiPIMS (b) Nb/Cu interface is shown in Fig. 6. This improvement should

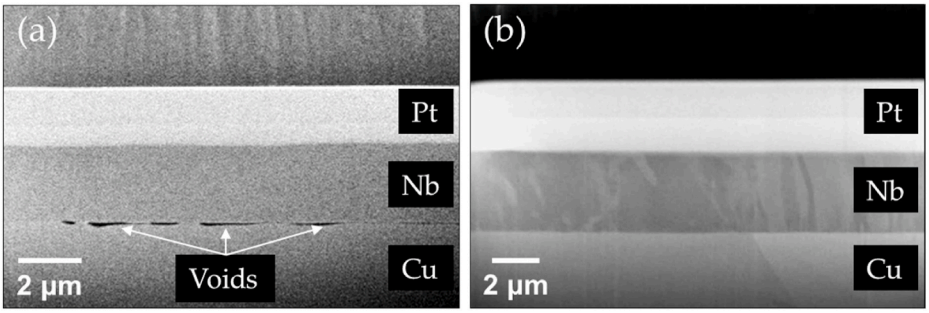

Fig. 6. SEM images detailing the Nb/Cu interface obtained with a FIB cut of (a) a DC MS Nb/Cu sample and (b) the base HiPIMS Nb/Cu sample. Samples deposited with the respective parameters detailed in Table 2.

greatly improve the thermal conductivity between the film and the substrate, thereby decreasing the influence of the thermal contact resistance [36]. Finally, the grain contrast observed in the SEM image of Fig. 6 (b) clearly shows the change in the Nb grain morphology across the Cu grain boundary. This indicates the reliance of the growth of Nb films on the Cu substrate, which is further detailed in Figs. 11 and 12 and expanded upon in their discussion.

3.3. Crystallographic analysis

With the exception of the high substrate bias sample, the results of the Bragg-Brentano (BB) XRD analyses of the Nb films are similar regardless of deposition parameter changes. As such, the normalised diffractogram of the base HiPIMS Nb film, which was deposited using the parameters detailed in Table 2, is plotted in log scale in Fig. 7. The diffractogram shows a pronounced increase in the relative intensity of the Nb (110) peak and a marked decrease in the relative intensities of all other Nb peaks, with respect to the relevant reference data, indicated by the green lines plotted in Fig. 7 (a) [37]. This result is similar to previous studies and indicates a polycrystalline Nb film with a preferred Nb (110) orientation [22,23]. An overarching feature in the diffractograms of all films is a shift in the Nb peak positions to lower diffraction angles compared to the bulk Nb reference position [37]. This is indicative of a compressive in-plane stress state in all films, leading to an increase in the out-of-plane lattice parameter.

Certain deposition parameters affected the crystal structure of the films more than others. With increasing substrate bias, the diffraction peaks displayed a continuously increasing shift to lower diffraction angles, signifying an increasing compressive in-plane stress in the films. This is shown in Fig. 7 (b) for increasing substrate bias. This results in an increase in the calculated out-of-plane lattice parameters of the films, the results of which are displayed in Fig. 8 (a). This is attributed to an increasing intensity of the atom peening mechanism [38], and the likely increased incorporation of the sputter gas species at higher values for the substrate bias. A similar shift in the diffraction peaks observed with increasing substrate temperature is due to the increased difference in thermal expansion between Nb and Cu at higher substrate temperatures. This also results in increase in the calculated out-of-plane lattice parameters, the results of which are presented in Fig. 8 (c). Within the investigated parameter space, the effects of the substrate bias on the lattice parameter are more significant than the substrate temperature.

Conversely, an increase in the deposition pressure leads to a decreased lattice parameter. This is presented in Fig. 8 (b), which shows a minimum of 3.3080 Å at 1.4×10^{-2} mbar, the closest value to bulk Nb achieved in this study. This trend has previously been shown for DC MS Nb films and is related to the decreasing mean free path associated with increasing deposition pressure and the subsequent decrease in the incident energy of the impinging adatoms and ionized species at the substrate surface [39].

Finally, increasing the film thickness resulted in a pronounced decrease in the lattice parameter between 0.9 and 1.8 μm. Above a thickness of 1.8 μm, a less pronounced decrease can be observed with a further increase of film thickness. This is displayed in Fig. 8 (d). A thicker film allows for stress relaxation by dislocation formation, which allows for a reduction of both the thermal stresses and the intrinsic stresses, due to the lattice mismatch of between Cu and Nb. No significant variations in lattice parameter were observed as a function of

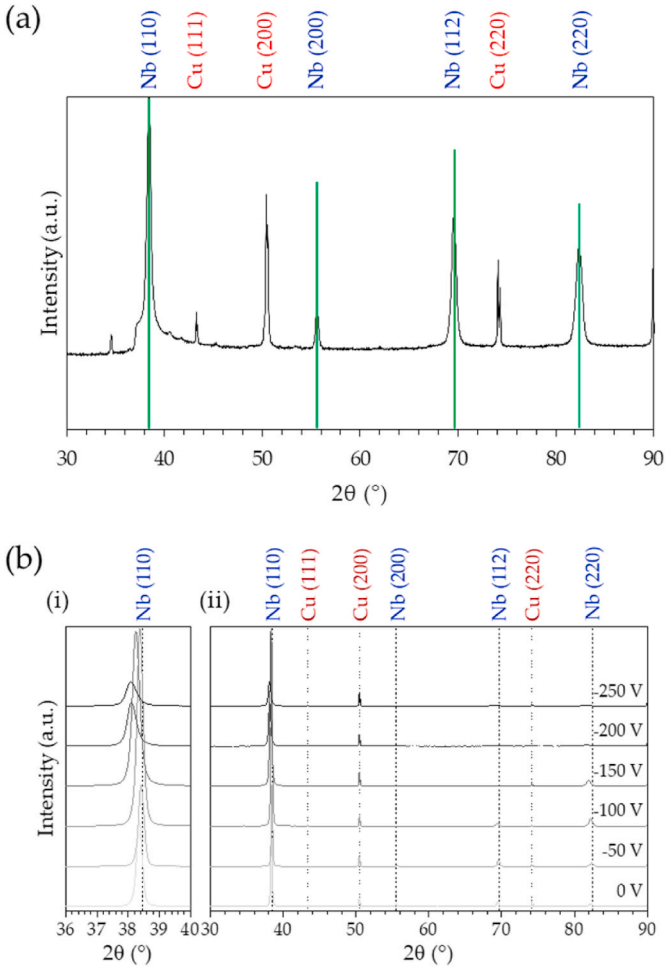

Fig. 7. (a) Normalised XRD spectrum of the HiPIMS Nb film deposited onto polycrystalline Cu using the parameters in Table 2, displayed in log scale. The normalised reference Nb diffractogram peak positions and relative intensities are displayed by the green lines, obtained from Ref. [37]. (b) XRD spectra of Nb films deposited with increasing substrate bias values, displayed in linear scale, with (i) displaying a magnified view of the main Nb (110) peak, allowing for better viewing of the peak broadening as well as peak displacement with increasing substrate bias, and (ii) displaying the full diffractograms.

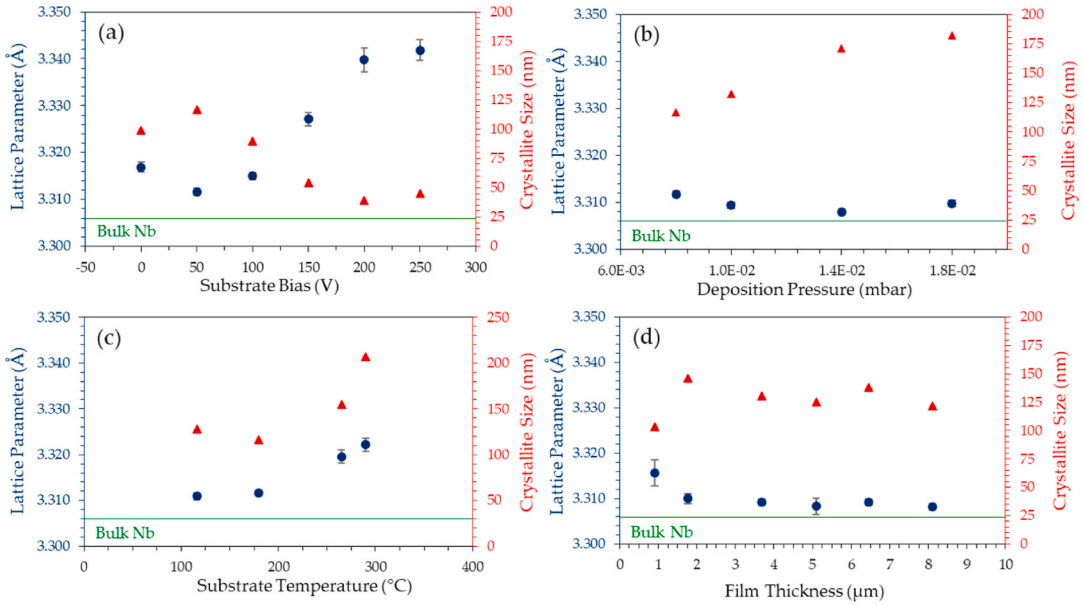

Fig. 8. Plots detailing the change in the lattice parameter and the average Nb (110) crystallite size as a result of (a) increasing substrate bias, (b) increasing deposition pressure, (c) increasing substrate temperature and (d) increasing film thickness. The reference for the bulk Nb lattice parameter (3.3060 Å) is indicated by the green line in all figures [37].

changes in the pulse length or frequency.

The XRD peaks themselves also display a significant broadening with increasing substrate bias, illustrated in Fig. 7 (b). This is accounted for by a decreasing crystallite size, determined by the Scherrer equation. During initial film growth stages, the high energy ions impacting the surface increase the likelihood of island formation by generating defect sites which are preferential nucleation sites, thereby restricting the crystallite size of the film. This is detailed in Fig. 8 (a), which indicates a decreasing crystallite size for increasing substrate bias values. Conversely, a noteworthy increase in crystallite size was observed for films deposited at higher substrate temperatures, owing to the activation of surface diffusion mechanisms. The largest crystallite size of all Nb films in this study (~207 nm) was produced at the highest substrate temperature used in this study, 290 °C. The relationship between the crystallite size and the substrate temperatures is plotted in Fig. 8 (c). A similar increase in crystallite size was observed with an increase in deposition pressure, as shown in Fig. 8 (b). Finally, Nb films of different thicknesses displayed a sharp initial increase in the crystallite size, followed by relatively consistent crystallite sizes for films thicker than 2 μm, as presented in Fig. 8 (d). This indicates a transition zone during the initial growth phase of the Nb films, most likely as a result of the selective growth model [40].

Of further interest is the relationship between the crystallite size and the lattice parameter of the deposited film, which is presented in Fig. 9. A nonlinear increase in the lattice parameter is observed with decreasing crystallite sizes in the deposited Nb films, with more bulk-like Nb observed for films consisting of larger crystallites. This is consistent with previous research on nanocrystalline Nb films and has been related to the excess free volume of grain boundaries [41] as well as the inhibition of dislocation motion [42] with smaller grain sizes.

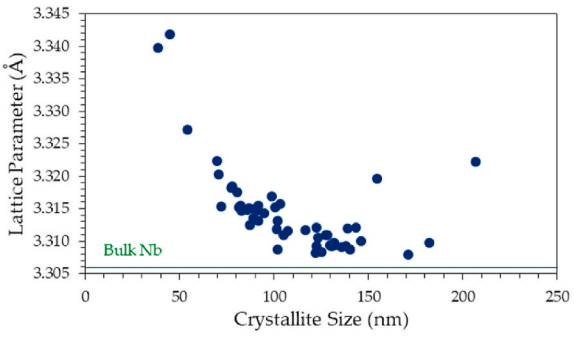

Fig. 9. Plot detailing the lattice parameter as a function of the crystallite size for all HiPIMS Nb thin films in this study.

In light of the orientation preference displayed in the BB scans, a series of pole figure (PF) investigations were undertaken to better understand the texture of the Nb film as well as the orientation relationship between the Cu substrate and the Nb film. This has previously been studied for Nb films deposited on single crystal Cu by Spradlin et al. [21] where specific epitaxial relationships between the deposited Nb films and the Cu substrates were observed; Nb (110)/Cu (100), Nb (110)/Cu (111) and Nb (100)/Cu (110).

The Cu (200) and Cu (111) PFs of a typical Cu substrate used in this study, not shown here, indicate a (200) preferred orientation for the Cu substrate, which is believed to be a result of the rolling process used during manufacturing. The PFs of the base HiPIMS Nb film, which was deposited using the parameters detailed in Table 2, are presented in Fig. 10. The pole figures, obtained at (a) $2\theta = 38.42°$, (b) $2\theta = 55.58°$ and (c) $2\theta = 69.53°$, represent the Nb (110), Nb (200) and Nb (112) orientations respectively. Due to the penetration depth of X-rays in Nb [43], these results represent the crystal structure averaged across the entire film thickness.

The Nb (110) PF displays an intense central spot with further satellites situated around the $\chi = 60°$ ring. These spots create a ring of modulated intensity in the azimuthal direction, pointing to a restricted fibre texture film, tending towards a monocrystalline film [44]. This is also indicative of the presence of an in-plane texture in the films. The 60° separation between the central spot and the satellite spots is due to the separation between the (110) and (101) planes in bcc crystals. The Nb (200) PF presents a further restricted spot pattern, with spots situated at 45°, providing further evidence for a restricted fibre texture. This 45° angle is due to the normal angle between the (110) and (200) planes. The observed intense central spot in the Nb (112) PF indicates a further orientation preference for these films and is consistent with the high intensity peak observed at $2\theta = 69.53°$ in Fig. 7.

The obtained Nb (110)/Cu (100) orientation relationship is typical

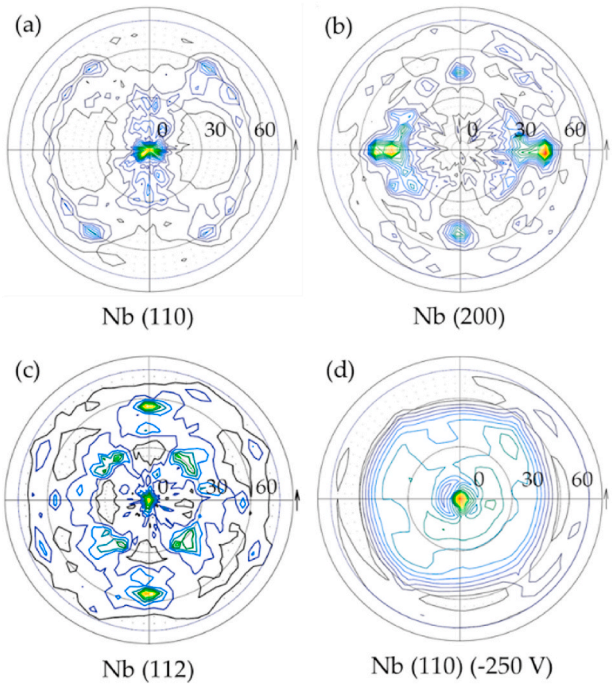

Fig. 10. Background corrected pole figures of the base HiPIMS Nb film for the (a) Nb (110) orientation, (b) Nb (200) orientation and (c) Nb (112) orientation. The sample was deposited with the parameters detailed in Table 2. Figure (d) shows the background corrected pole figure of a HiPIMS Nb film deposited with equal deposition parameters to (a–c), albeit with a -250 V substrate bias.

for both DC MS [43] and energetically deposited Nb films on Cu (100) substrates [21,45]. Moreover, this is the typical out-of-plane orientation for bcc materials [46]. However, an in-plane texture in the Nb films is believed to be due to the use of energetic deposition techniques, such as HiPIMS (this study), CED™ [45,47] or ECR [21]. The appearance of in-plane texture has also previously been shown for Ion-Beam-Assisted Deposition (IBAD) of Nb films [8,44]. However, these films were deposited with off-normal ion incidence angles and higher ion energies (200 – 1000 eV). The mechanism behind the in-plane texture formation in these films was stated to be due to ion-channelling along planes closely aligned to the ion beam direction, resulting in faster growth rates of these orientations.

On the other hand, films in this study were deposited with lower ion energies of ~ 50 eV and a 90° ion arrival angle with respect to the substrate surface. Because of the low energies used here, and the angle of incidence of the ions, this is likely not as a result of ion channelling, as seen in IBAD films. Instead, the increased energy provided by the ions likely promotes long-range-order in the crystal structure due to enhanced adatom mobility during film growth, as previously mentioned by Zhao et al. [48].

The recorded PF results for all deposited films were similar to the PFs shown in Fig. 10 (a–c), except for those deposited at higher substrate biases, which indicated a loss of in-plane texture with increasing substrate bias, as evidenced by a transition from a spot pattern to an azimuthally distributed ring pattern at 60°. This is visible in the PF of the Nb film deposited at -250 V substrate bias which is displayed in Fig. 10 (d). With increased ion energy, the crystalline structure is disturbed due to the creation of defects, indicated by a decreased crystallite size in Fig. 8 (a), resulting in the loss of in-plane texture.

The crystallographic texture of a series of Nb films were additionally investigated with EBSD, which details the crystallographic identity of the top 50 – 100 nm of a sample and is therefore more representative of the surface orientation than PF measurements [49]. The surfaces of four separate samples were analysed with EBSD, both before (Cu surface) and after (Nb film surface) film deposition, in order to further understand their orientation relationship. The OIMs and Inverse Pole Figures (IPFs) of the surface of two separate Nb/Cu samples (a) prior to (Cu substrate) and (b) after deposition (Nb film) are displayed in Fig. 11. The deposition parameters used were the same as those depicted in Table 2, albeit with an increased pulse length of 120 μs. The analysis of the Cu substrate yielded an average Confidence Index (CI) of 0.82 while that of Nb was 0.79.

Based on Fig. 11, and consistent with the XRD and PF results, the films are polycrystalline in nature with separate positions on the Nb film surface displaying preferred (110) and (112) orientations. A more pronounced grouping around the (110) orientation is observed in the corresponding Nb film IPF's, consistent with the continuously higher intensity of this peak in BB XRD scans. The further two samples, which were deposited with the same deposition parameters, echoed these results. As such, they are not displayed here. This result is in line with work completed by previous authors [13,22]. The Nb/Cu orientation relationship on polycrystalline Cu substrates also appears to be less restricted than the specific Nb/Cu orientation relationships previously reported for Nb deposition on single crystal Cu substrates [21]. Further to this, the grain boundaries in the Nb films do not align with those of the underlying Cu substrate, indicating grain expansion and overgrowth of the deposited Nb film. Therefore, due to the thickness of the films (> 2 μm) the surface of the Nb films is likely not representative of the epitaxial relationship of Nb and Cu at the interface. The distribution of Nb grain sizes is further apparent in these images, with the films constituted by regions of either small (100's of nm) or large (μm) scale grains, with very few regions in between.

In order to better understand the growth of the Nb films, a series of sample cross sections were analysed with EBSD and the resultant OIMs are displayed in Fig. 12. Three positions on two separate samples were analysed. The deposition parameters of these samples were the same as those shown for the HiPIMS film depicted in Table 2, albeit with an increased pulse length of 120 μs for (a) and (b), and an increased deposition time in the case of (c).

The growth of the Nb films show instances of reliance on the underlying Cu substrate, though it is not strictly dictated by the Cu substrate. In position (a), at the interface, the Nb film shows zone T-like growth, with competitive growth of crystallites of different orientations. Once the dominant orientation has overgrown the others, a more columnar-like growth takes over. As such, we see the grain size increasing with increasing film thickness, resulting in the loss of the Cu substrate topography on the surface of the film, as detailed in Fig. 11. This also follows the proposed selective growth model, whereby grains with different crystal orientations have different growth rates based on their thermodynamic potentials [40]. On the other hand, position (b) indicates the potential for grain growth on the order of the film thickness, resulting in grain sizes on the order of micrometres with HiPIMS. A change in the Nb film orientation is observed to coincide with the changing Cu orientation at the Cu grain boundary, though this could also be due to changing surface morphology of the Cu substrate. Finally, position (c) indicates the possibility to have two dissimilar grain morphologies on a single Cu grain, further decreasing the likelihood of Cu grain replication in the overgrown Nb film.

There are two mechanisms involved here, namely: defect introduction and the native surface morphology. Firstly, with energetic condensation techniques such as HiPIMS, the impacting adatoms can create defects, which act as preferential growth sites. The new nucleus doesn't necessarily have a heteroepitaxial relationship with the substrate. Secondly, the morphology of the Cu grain plays an important role in nucleation. Defects within the Cu grain, such as edge dislocations, can lead to different orientations. Both mechanisms promote Volmer-Weber growth mode with small lateral grain dimensions at the interface. In the absence of defects, whether induced or native, a Volmer-Weber growth mode is still present but due to the high diffusion length of high energy Nb adatoms on a defect free Cu surface, the lateral grain dimension is

increased to μm as shown in the EBSD analysis. This also dispels the possibility of there being a single Nb/Cu orientation relationship when deposited on polycrystalline Cu substrates. Based on the above, the Nb films grown here appear to be in the transition region between zone-T and zone 2 type growth depicted in the Structure Zone Diagram (SZD) proposed by Anders [9]. Finally, the transition zone introduced with Fig. 8 (d) is also clearly visible in (a) and (c), where the interfacial grains are significantly smaller than those at the film surface.

Fig. 13 (a) shows a cross-sectional bright field TEM image from a section of the best performing Nb/Cu sample, in terms of entry field, from this study. This sample was deposited with the same parameters as those depicted in Table 2, albeit with a longer pulse length of 120 μs. A columnar structure is observed in the Nb film in which the Nb grains are inclined approximately 12° relative to the interface normal between substrate and film. The width of the Nb columnar grains ranges from a few tens of nanometre to about one micron. No voids have been found at the interface, as already indicated by the SEM image in Fig. 6 (b). This indicates the potential for a reduced thermal contact resistance due to the improved adhesion between the Nb film and the Cu substrate.

The contrast in the bright field TEM image is dominated by diffraction contrast. Therefore, the similar contrast of several grains in the image indicates a similar orientation and therefore also a predominant growth orientation in the Nb film. According to selected area electron diffraction, the orientation of those grains along the viewing direction is parallel to Nb [111], as can be seen from the diffraction pattern in Fig. 13 (b). Moreover, the Cu [110] zone axis of the Cu substrate was almost parallel to the viewing direction with a 3° difference in tilt angle. The crystallographic relationship between the two zone axes, Nb [111] and Cu [110], is shown in Fig. 13 (d).

The film orientation, i.e. the orientation perpendicular to the interface, of the Nb film was found to be parallel to Nb [$\bar{3}4\bar{1}$]. This film orientation corresponds well to the top-view EBSD measurements of the Nb film shown in Fig. 11 (b), in which the grain characterised by TEM would appear in light green in the IPF. This orientation is also exhibited by a large fraction of the Nb grains investigated by EBSD. However, taking into account the inclination of the grains in Bragg condition (dark grains) to the interface normal and relating the image to the diffraction patterns indicates that the growth direction of the Nb grains to be closer to Nb < 112>. The {112} surface plane of fcc metals is known to possess a relatively low surface energy [50–53]. Thus, observation and surface facet energies suggest this direction to be energetically favoured, as indicated by the PF shown in Fig. 10 (c) as well.

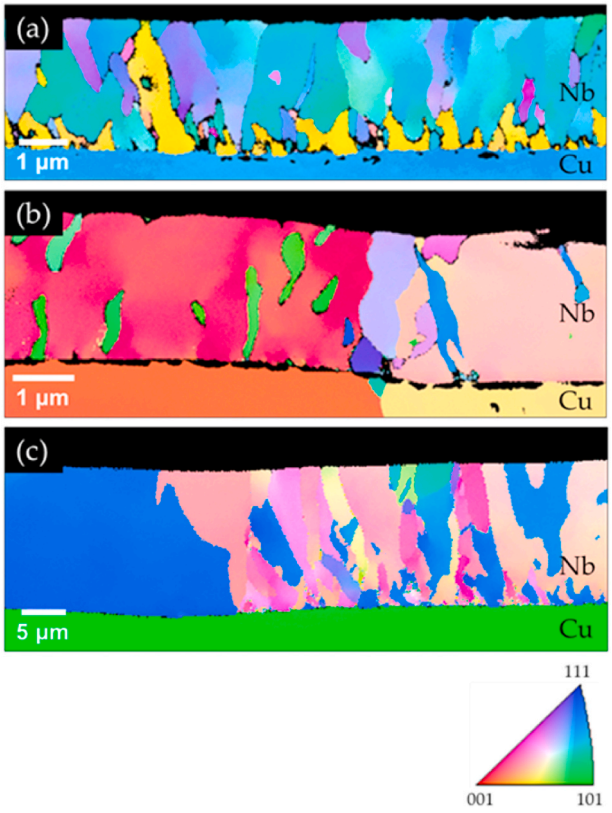

Fig. 12. EBSD OIMs of the cross section of the HiPIMS Nb/Cu sample deposited with parameters detailed in Table 2, albeit with a 120 μs pulse length. The image displays two separate positions which show (a) selective growth through the thickness and (b) individual grain growth through the thickness. (c) Further OIM of the thickest Nb film sample displaying two separate grain growth phenomena on a single Cu grain.

The diffraction pattern of Cu in Fig. 13 (c) shows that the Cu < 112> orientation is close to the Nb < 112> growth direction. Comparing the

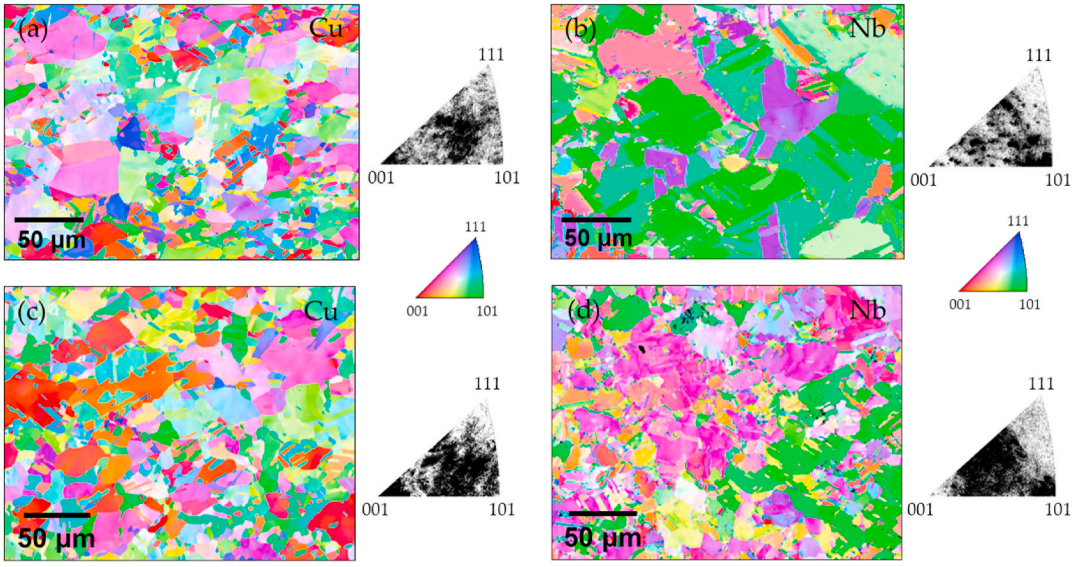

Fig. 11. EBSD Orientation Index Maps (OIMs) and the corresponding Inverse Pole Figures (IPFs) of two separate Nb/Cu samples deposited with parameters detailed in Table 2, albeit with a 120 μs pulse length. Images (a) and (c) depict the Cu substrate surface before deposition, while (b) and (d) depict the deposited Nb film surface in the same position.

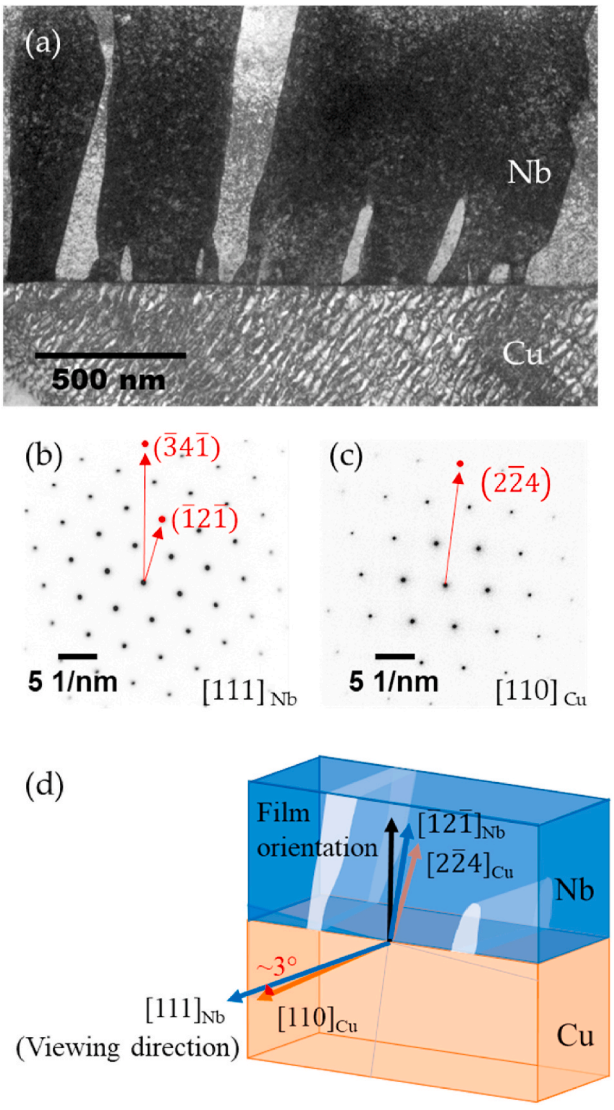

Fig. 13. (a) Bright field TEM image of the cross section of the HiPIMS Nb/Cu sample deposited with parameters detailed in Table 2, albeit with a 120 μs pulse length. One set of Nb grains is oriented in zone axis such that they appear dark in the bright-field image. (b) and (c) Selected-area electron diffraction pattern of the Nb film and Cu substrate. (d) Spatial relationship between zone axis Nb [111] and Cu [110].

diffraction patterns in Fig. 13 (b) and (c), it can be seen that there is a small misorientation between the two <112> directions of the substrate and the film. The origin of this misorientation is attributed to the lattice misfit between Cu and Nb in those orientations (~ 9 %) and the resulting energy minimisation of the interface. Nevertheless, the TEM results suggest a direct epitaxial relation between the substrate and film for this specific TEM sample.

Moreover, the results discussed above are also in good agreement with the cross-section EBSD measurements shown in Fig. 12 (c) (left side) where the orientations of the Cu substrate and the Nb film were also found to be Cu < 110> and Nb < 111>.

3.4. Superconducting property analysis

Sections of all samples, 2 × 2 mm^2 in size, were tested in a VSM to determine their transition temperature (T_c) and entry field ($\mu_0 H_{en}$) values. The critical temperature of these samples was measured during cooldown and is taken as the onset of the change in magnetic moment (m) while the transition width (ΔT_c) is taken as 80 % of the difference between the onset of change in the magnetic moment and the constant magnetic moment plateau.

The majority of the samples displayed similar T_c values of 9.31 ± 0.06 K, slightly above bulk Nb. This is as a result of the compressive in-plane stresses detailed earlier. The films also feature a relatively consistent ΔT_c of 0.19 ± 0.05 K, which is related to the small changes in the lattice parameter values of the films. However, two sets of films, those deposited with increasing substrate bias (-50 to –250 V) and increasing substrate temperature (116 – 290 °C), displayed pronounced changes to their T_c values, increasing to 9.7 K (≥ -150 V) and 9.6 K (290 °C) respectively, while their ΔT_c. Values rose to 0.68 and 0.40 K respectively, indicating the increased state of stress and increased presence of defects, such as dislocations, within the films. These results correlate well with the calculated lattice parameters displayed in Fig. 8.

The magnetisation loops of all samples were also recorded after cooling down the sample in zero applied magnetic field. The applied field was then linearly increased from 0 to 1 T, recording the so-called virgin magnetisation curve. Then the applied field was inverted, decreasing linearly from 1 T through 0 to −1 T and afterwards increasing back to 1 T, recording the full magnetisation loop. The magnetisation curves allowed for determination of the entry field ($\mu_0 H_{en}$), trapped flux density ($\mu_0 H_{tr}$) and maximum field ($\mu_0 H_p$). The entry field was identified by the deviation of the magnetic moment from the initial linear trend observed in the virgin curve, employing a 2 % relative difference criterion. It correlates with the first critical field of the superconductor (H_{c1}), in the absence of pinning, and if no sample shape factors were involved, one would have $H_{en} = H_{c1}$. The trapped flux density is indicated by the y-intercept of the reverse loop and the maximum field, which is proportional to the full penetration field through a geometrical shape factor, corresponds to the field at which the minimum magnetic moment (maximum in absolute value) is reached on the virgin curve [54]. The full penetration field itself marks the field at which the magnetic flux penetrates the whole volume of the superconductor. It is determined by the strength of the bulk pinning in the superconductor volume, in an ideal pinning-free sample one would have $H_p = H_{c1}$ (disregarding the shape factors). The measurements were conducted at 4.22 K, in a field applied parallel to the sample surface. For the sake of brevity, only a part of the normalised magnetisation loops for the samples deposited with increasing substrate bias and film thickness values are presented in Fig. 14 (a) and (c).

The characteristic dip in the reverse section of the magnetisation loop encountered at ~ 120 mT is a result of the surface barrier effects in combination with the reversible magnetisation curve [55]. The size of the dip is seen to decrease with increasing substrate bias, becoming a simple kink at -100 V and disappearing above -150 V. This is likely due to the surface damage at higher substrate bias values, as detailed in Fig. 4 (f). The trapped flux in the films, indicated by the size of the hysteresis loops, also increases steadily with increasing substrate bias values. This is likely due to increased flux pinning as a result of an increase in dislocation density, indicated by a decrease in the crystallite size of the films. The decrease in crystallite size of the Nb films, which is observed with an increase in the substrate bias, is presented in Fig. 8 (a). In spite of the increased hysteresis loop size, and therefore increase in trapped flux, the sample deposited at -100 V substrate bias displayed the largest entry field value of $\mu_0 H_{en}$ = 79 mT, for samples deposited with varying bias. This was determined from the deviation of m/m_i from the constant value of 1 in Fig. 14 (b), where m_i denotes the initial linear section of the virgin curve $m_i = cH_a$, corresponding to the Meissner shielding state (c – constant, H_a – applied field). The reason could be due to the strong pinning at the film surface, which can result in the measured virgin curve running very close to the linear Meissner trend line even after the start of field penetration into the film.

With further increase of the substrate bias, more defects are produced than annihilated, leading to a significant decrease in the entry field value, as displayed by the earlier m/m_i deviation in the plotted data

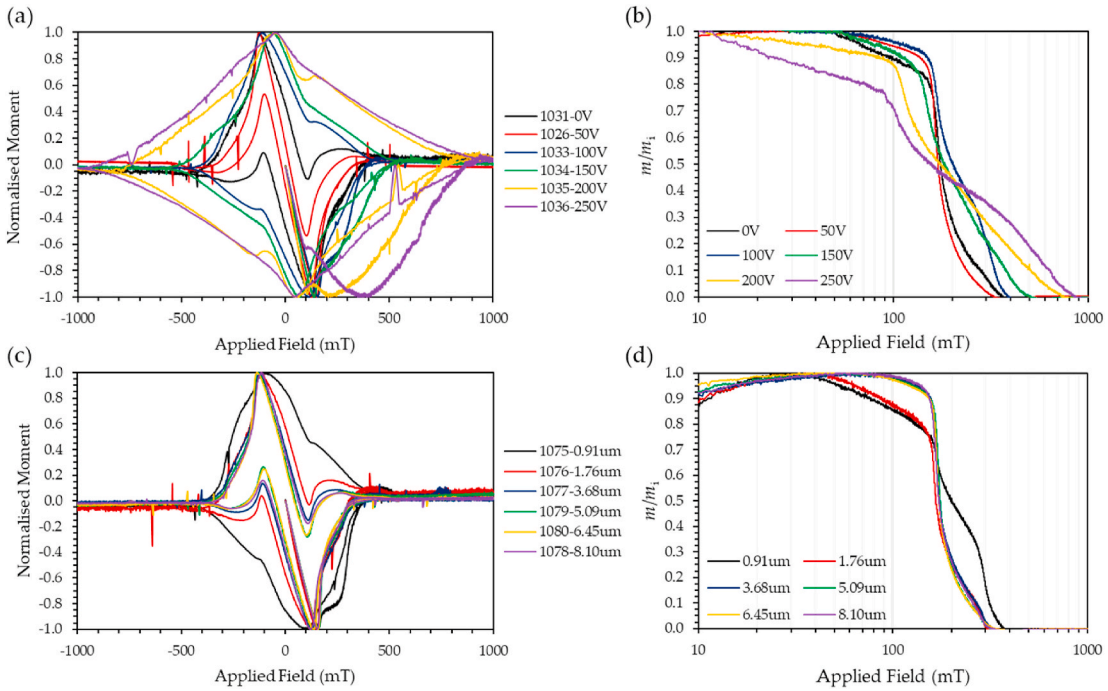

Fig. 14. Normalised magnetisation loops ((a) and (c)) and the virgin curves normalised to their initial linear sections m_i ((b) and (d)), for the Nb samples deposited with, (a) and (b), increasing substrate bias values as well as samples deposited with, (c) and (d), increasing film thickness values. The measurements were conducted at 4.22 K. The lower, positive-valued curves in (a) and (c) represent the virgin magnetisation curves, recorded sweeping the applied field from 0 to +1 T. The upper curves are portions of the reverse loops recorded sweeping the applied field back from +1 T to -1T. Finally, the lower, negative-valued curve displays the applied field swept from -1 T to 0 T.

in Fig. 14 (b) and the corresponding decrease of $\mu_0 H_{en}$ in Fig. 15 (a). This is supported by the decreased surface quality at -250 V shown in Fig. 4 (f).

The normalised magnetisation loops recorded for films of different thicknesses, presented in Fig. 14 (c), display a noteworthy decrease in the relative size of the loops and a subsequent decrease in the trapped flux with increasing film thickness, except for the thickest film, which shows an anomalously high trapped flux value. This decrease is likely linked to a reduction of the dislocation density in the film region penetrated by the magnetic field and a more coherent grain structure

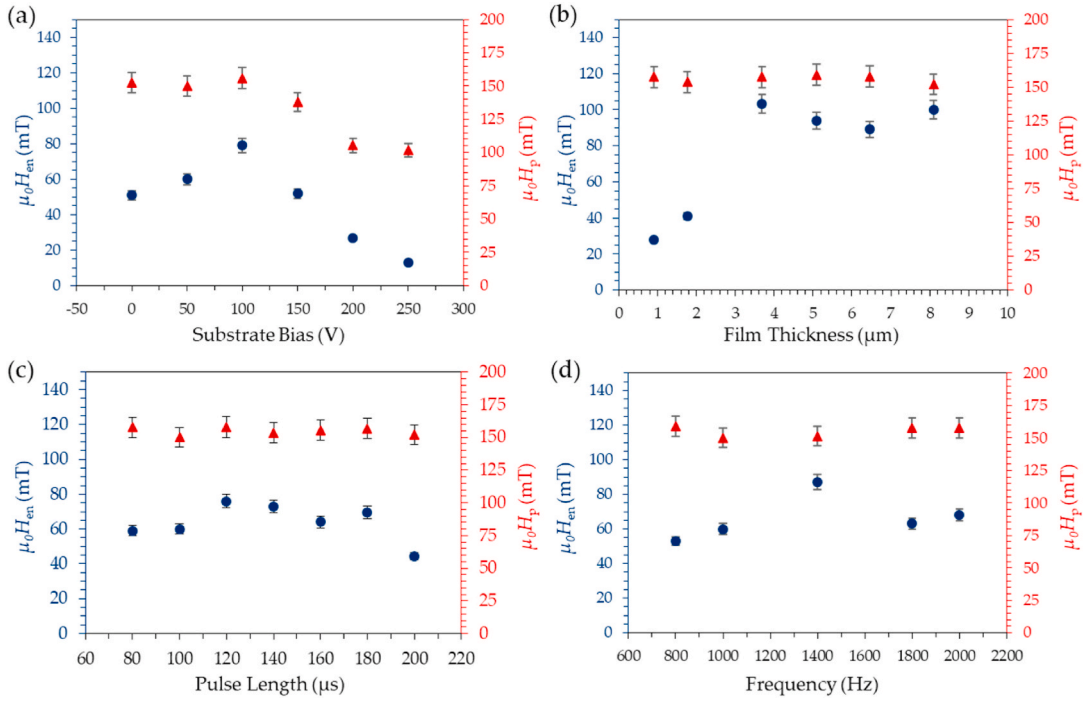

Fig. 15. Plots detailing the change in the entry field ($\mu_0 H_{en}$) and the maximum field ($\mu_0 H_p$), measured in a parallel applied field, as a function of: (a) substrate bias, (b) film thickness, (c) pulse length and (d) frequency.

with increasing film thickness. This is indicated by a pronounced increase in the crystallite size between a film thickness of 0.91 and 1.76 μm, observed in the XRD results plotted in Fig. 8 (d) and the cross section EBSD images in Fig. 12. Increasing the film thickness to ≥ 1.8 μm also leads to the emergence of the dip in the reverse magnetisation loop at an applied field of ~ 120 mT.

The m/m_i ratio, displayed in Fig. 14 (d), is similar for film thicknesses ≥ 3.68 μm, providing further evidence for the initial transition zone in the deposited Nb films. As detailed in Fig. 15 (b), the film with a thickness of 3.68 μm exhibited the highest entry field value during these individual parameter studies, with $\mu_0 H_{en} = 103$ mT, nearly twice as high as the field found for previous DC MS coatings [7]. However, this value is still significantly lower than the purported $H_{c1} = 160$ mT for small Nb samples [55]. This is likely related to the geometrical edge effects associated with the full immersion of the samples in the magnetic field during testing [23,56].

Of particular interest in this study was whether or not the use of a higher HiPIMS duty cycle would negatively affect the superconducting properties of the Nb films, due to the decreased ionisation of sputtered Nb particles. As shown in Fig. 15(c) and (d), the effect of the duty cycle, i.e. the pulse length or pulse frequency, on the entry field and the maximum field is insignificant in comparison to the effect of substrate bias and film thickness. For changes in both the pulse length and the frequency, films coated at 12 or 14 % duty cycle display superior entry field values, though the variation is more apparent for changes in the pulse frequency. On the other hand, the maximum field value shows no significant dependence on the duty cycle.

It is evident that films whose crystal structure approaches that of unstressed, bulk Nb have better superconducting performance, as summarised for all films in Fig. 16. As such, given the relationship between the crystallite size and lattice parameter displayed in Fig. 9, further increases in the crystallite size may provide a route to further improve the performance of Nb thin films.

4. Conclusion

A series of Nb films have been deposited onto electropolished OFE Cu substrates using HiPIMS. The results show a more pronounced influence on the superconducting performance by three specific deposition parameters: the substrate temperature, substrate bias and film thickness, while the cathode power, deposition pressure, pulse length and pulse frequency show a comparatively lower influence.

The observed changes in the superconducting performance are shown to be related to changes in the crystallographic structure of the Nb film, its state of stress and the resultant grain morphology within the penetration depth of the RF field. Evidently, Nb films with more bulk-like lattice parameters and larger crystallite sizes show improved superconducting performance. These characteristics are typically found in films thicker than ~ 3.5 μm, which also presented a more coherent grain structure and decreased film stress, resulting in better entry field values, smaller magnetisation loops and subsequent lower levels of trapped flux.

Within the investigated parameter space, changes to the duty cycle did not result in any significant changes to the crystallographic structure of the films. It must be mentioned that, as a result of the substrate bias values and the short target to substrate distance in this work, this is valid for low/moderate Nb ion energies. Further to this, in spite of the relative entry field maximums obtained during superconducting testing, changes to the duty cycle do not appear to be a significant pathway to superconducting performance improvements of Nb thin films. Nevertheless, increasing the duty cycle also allows for operation at lower deposition pressures, which results in lower gas entrapment in the deposited films, not fully investigated here. This needs to be balanced with the desired ionisation of the sputtered material however.

In light of these results, films used for srf cavities, in either single or multilayer structures, should be deposited at an intermediate temperature with a relatively low substrate bias and at thicknesses between 3 and 6 μm, to restrict the increasing surface roughness observed at higher film thicknesses. In addition, a lower average cathode power is recommended, in order to increase the crystallite size and decrease the resultant surface roughness by allowing sufficient time for surface diffusion.

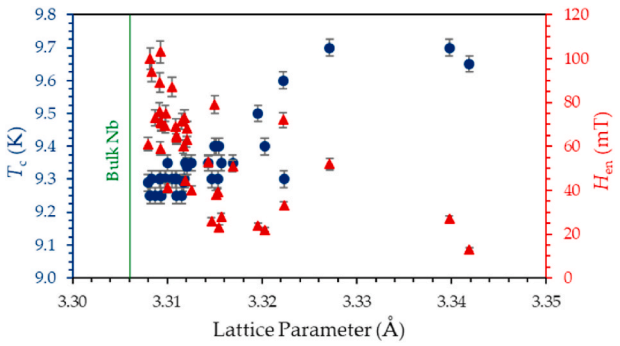

Fig. 16. Variation of the transition temperature and entry field of all HiPIMS Nb thin films in this study as a function of the lattice parameter.

CRediT authorship contribution statement

S. Leith: Writing – review & editing, Writing – original draft, Project administration, Methodology, Investigation, Formal analysis, Data curation, Conceptualization. **J. Qiao:** Investigation, Data curation. **M. Vogel:** Writing – review & editing, Validation, Supervision, Resources, Project administration, Funding acquisition, Conceptualization. **E. Seiler:** Writing – review & editing, Writing – original draft, Formal analysis, Data curation. **R. Ries:** Writing – review & editing, Data curation. **Y. Li:** Writing – original draft, Investigation, Formal analysis, Data curation. **C. Wiktor:** Writing – review & editing, Writing – original draft, Resources, Investigation, Formal analysis, Data curation. **J. Mueller:** Writing – review & editing, Writing – original draft, Resources, Investigation, Formal analysis, Data curation. **Y. Sakalli:** Resources, Methodology, Investigation. **B. Butz:** Writing – review & editing, Resources, Investigation. **X. Jiang:** Writing – review & editing, Supervision, Resources, Funding acquisition.

Declaration of competing interest

The authors declare that they have no known competing financial interests or personal relationships that could have appeared to influence the work reported in this paper.

Data availability

Data will be made available on request.

Acknowledgements

The synthesis and materials characterization in this work forms part of the EASITrain Marie Sklodowska-Curie Action (MSCA) Innovative Training Networks (ITN) which has received funding from the European Union's H2020 Framework Programme under Grant Agreement no. 764879.

The characterisation of the superconducting properties in this work forms part of the European Union's ARIES collaboration H2020 Research and Innovation Programme under Grant Agreement no. 730871.

Part of this work was performed at the DFG-funded Micro-and Nanoanalytics Facility (MNaF) of the University of Siegen (INST 221/131-1) utilising its major TEM instrumentation (DFG INST 221/93-1, DFG INST 221/126-1), FIB-SEM and sample preparation equipment.

Special thanks to G. Rosaz from CERN for assisting with the XRF thickness measurements of these films and valuable discussions.

References

[1] C. Benvenuti, D. Bloess, E. Chiaveri, N. Hilleret, M. Minestrini, W. Weingarten, Superconducting cavities produced by magnetron sputtering of niobium on copper, in: Proceedings of 3rd Workshop on RF Superconductivity, SRF 1987), 1987, pp. 445–468.

[2] S. Calatroni, 20 Years of experience with the Nb/Cu technology for superconducting cavities and perspectives for future developments, Phys. C Supercond. its Appl. 441 (1–2) (2006) 95–101, https://doi.org/10.1016/j.physc.2006.03.044.

[3] C. Benvenuti, S. Calatroni, M. Hakovirta, H. Neupert, M. Prada, A. Valente, CERN studies on niobium-coated 1 . 5 GHz copper cavities, in: Proceedings of 10th Workshop on RF Superconductivity, SRF 2001), 2001, pp. 252–258.

[4] C. Benvenuti, et al., Study of the surface resistance of superconducting niobium films at 1.5 GHz, Phys. C Supercond. its Appl. 316 (3–4) (May 1999) 153–188, https://doi.org/10.1016/S0921-4534(99)00207-5.

[5] C. Benvenuti, S. Calatroni, P. Darriulat, M.A. Peck, A.-M. Valente, C.A.V. Hof, Study of the residual surface resistance of niobium films at 1.5 GHz, Phys. C Supercond. its Appl. 351 (4) (2001) 421–428, https://doi.org/10.1016/S0921-4534(00)01645-2.

[6] B. Visentin, Review on Q-DROP mechanisms, in: 2nd International Workshop on Thin Films and New Ideas for Pushing the Limits of RF, 2006, pp. 1–5.

[7] S. Leith, M. Vogel, J. Fan, E. Seiler, R. Ries, X. Jiang, Superconducting NbN thin films for use in superconducting radio frequency cavities, Supercond. Sci. Technol. 34 (2) (Feb. 2021), 025006, https://doi.org/10.1088/1361-6668/abc73b.

[8] H. Ji, G.S. Was, J.W. Jones, N.R. Moody, Effect of ion bombardment on in-plane texture, surface morphology, and microstructure of vapor deposited Nb thin films, J. Appl. Phys. 81 (10) (May 1997) 6754–6761, https://doi.org/10.1063/1.365217.

[9] A. Anders, A structure zone diagram including plasma-based deposition and ion etching, Thin Solid Films 518 (15) (2010) 4087–4090, https://doi.org/10.1016/j.tsf.2009.10.145.

[10] G. Wu, et al., Studies of niobium thin film produced by energetic vacuum deposition, Thin Solid Films 489 (1–2) (Oct. 2005) 56–62, https://doi.org/10.1016/j.tsf.2005.04.099.

[11] R. Russo, L. Catani, A. Cianchi, S. Tazzari, J. Langner, High quality superconducting niobium films produced by an ultra-high vacuum cathodic arc, Supercond. Sci. Technol. 18 (7) (Jul. 2005) L41–L44, https://doi.org/10.1088/0953-2048/18/7/L01.

[12] L. Catani, et al., Recent achievements in ultra-high vacuum arc deposition of superconducting Nb layers, Proc. SPIE 5 (Oct. 2007), https://doi.org/10.1117/12.784584.

[13] X. Zhao, et al., Large crystal grain niobium thin films deposited by energetic condensation in vacuum arc, J. Vac. Sci. Technol. A Vacuum, Surfaces, Film. 27 (4) (Jul. 2009) 620–625, https://doi.org/10.1116/1.3131725.

[14] A. Anders, et al., Deposition of niobium and other superconducting materials with high power impulse magnetron sputtering: concept and first results, Proceedings of 15th International Conference on RF superconductivity (2011) 302–308. SRF 2011.

[15] G. Terenziani, S. Calatroni, T. Junginger, I.A. Santillana, S. Sheffield, Nb coating developments with HiPIMS for SRF applications, in: Proceedings of 16th International Conference on RF Superconductivity, SRF 2013), 2013, pp. 621–624.

[16] M. Burton, et al., RF results of Nb coated srf accelerator cavities via HiPIMS, in: Proceedings of 18th International Conference on RF Superconductivity, SRF, 2017, pp. 535–538, https://doi.org/10.18429/JACoW-SRF2017-TUPB066, 2017.

[17] G. Rosaz, Nb/Cu studies at CERN, FCC Week (2018), 2018.

[18] C.Z. Antoine, Influence of crystalline structure on rf dissipation in superconducting niobium, Phys. Rev. Accel. Beams 22 (3) (Mar. 2019), 034801, https://doi.org/10.1103/PhysRevAccelBeams.22.034801.

[19] W.M. Roach, et al., Niobium thin film deposition studies on copper surfaces for superconducting radio frequency cavity applications, Phys. Rev. Spec. Top. Accel. Beams 15 (6) (2012) 1–6, https://doi.org/10.1103/PhysRevSTAB.15.062002.

[20] S. Calatroni, C. Benvenuti, P. Darriulat, M.A. Peck, A. Valente, S. Calatroni, Influence of the Nature of the Substrate on the Growth of Superconducting Niobium Films, CERN-EST-2000-005-SM, 2000.

[21] J. Spradlin, et al., Structural properties of niobium thin films deposited on metallic substrates, in: Proceedings of 15th International Conference on RF Superconductivity, SRF, 2011, pp. 877–882, 2011.

[22] M. Burton, A. Palczewski, A.M. Valente-Feliciano, C.E. Reece, Progress with Nb HiPIMS films on 1.3GHz Cu cavities, in: Proceedings of 19th International Conference on RF Superconductivity, SRF, 2019, pp. 823–827, https://doi.org/10.18429/JACoW-SRF2019-THFUB2, 2019.

[23] S. Wilde, R. Valizadeh, O.B. Malyshev, G.B.G. Stenning, T. Sian, B. Chesca, Dc magnetometry of niobium thin film superconductors deposited using high power impulse magnetron sputtering, Phys. Rev. Accel. Beams 21 (7) (Jul. 2018), 073101, https://doi.org/10.1103/PhysRevAccelBeams.21.073101.

[24] A.-M. Valente-Feliciano, HiPIMS : a new generation of film deposition techniques for srf applications, in: Proceedings of 16th International Conference on RF Superconductivity, SRF 2013), 2013, pp. 754–760.

[25] O. Kugeler, et al., ARIES Deliverable Report D15.3: Evaluation of System 3 and SIS, 2020 [Online]. Available: https://edms.cern.ch/document/1820619/1.0%0A.

[26] B. Gale, D. Griffiths, Influence of instrumental aberrations on the schultz technique for the measurement of pole figures, Br. J. Appl. Phys. 11 (3) (Mar. 1960) 96–102, https://doi.org/10.1088/0508-3443/11/3/302.

[27] C. Pira, et al., Impact of the Cu substrate surface preparation on the morphological, superconductive and rf properties of the Nb superconductive coatings, in: Proceedings of 19th International Conference on RF Superconductivity, SRF, 2019, pp. 937–942, https://doi.org/10.18429/JACoW-SRF2019-THP041, 2019.

[28] A.P. Ehiasarian, R. New, W.-D. Münz, L. Hultman, U. Helmersson, V. Kouznetsov, Influence of high power densities on the composition of pulsed magnetron plasmas, Vacuum 65 (2) (Apr. 2002) 147–154, https://doi.org/10.1016/S0042-207X(01)00475-4.

[29] J. Alami, S. Bolz, K. Sarakinos, High power pulsed magnetron sputtering: fundamentals and applications, J. Alloys Compd. 483 (1–2) (Aug. 2009) 530–534, https://doi.org/10.1016/j.jallcom.2008.08.104.

[30] K. Sarakinos, J. Alami, S. Konstantinidis, High power pulsed magnetron sputtering: a review on scientific and engineering state of the art, Surf. Coating. Technol. 204 (11) (Feb. 2010) 1661–1684, https://doi.org/10.1016/j.surfcoat.2009.11.013.

[31] G. Greczynski, L. Hultman, Peak amplitude of target current determines deposition rate loss during high power pulsed magnetron sputtering, Vacuum 124 (Feb. 2016) 1–4, https://doi.org/10.1016/j.vacuum.2015.11.004.

[32] A. Anders, Discharge physics of high power impulse magnetron sputtering, Surf. Coating. Technol. 205 (Jul. 2011) S1–S9, https://doi.org/10.1016/j.surfcoat.2011.03.081.

[33] J.T. Gudmundsson, N. Brenning, D. Lundin, U. Helmersson, High power impulse magnetron sputtering discharge, J. Vac. Sci. Technol. A Vacuum, Surfaces, Film. 30 (3) (May 2012), 030801, https://doi.org/10.1116/1.3691832.

[34] M.a. Mantenieks, Sputtering threshold energies of heavy ions, NASA Tech. Memo. 2 (June) (1999), 209273.

[35] W. Tan, et al., Superiority of high power impulse magnetron sputtering in niobium films deposition on copper, Mater. Res. Express 6 (2) (Nov. 2018), 026418, https://doi.org/10.1088/2053-1591/aaeefe.

[36] V. Palmieri, R. Vaglio, Thermal contact resistance at the Nb/Cu interface as a limiting factor for sputtered thin film RF superconducting cavities, Supercond. Sci. Technol. 29 (1) (2015), https://doi.org/10.1088/0953-2048/29/1/015004.

[37] ICSD File 645059 (2008).

[38] H. Windischmann, Intrinsic stress in sputter-deposited thin films, Crit. Rev. Solid State Mater. Sci. 17 (6) (Jan. 1992) 547–596, https://doi.org/10.1080/10408439208244586.

[39] C.T. Wu, Intrinsic stress of magnetron-sputtered niobium films, Thin Solid Films 64 (1) (Nov. 1979) 103–110, https://doi.org/10.1016/0040-6090(79)90549-2.

[40] A. van der Drift, Evolutionary selection, a principle governing growth orientation in vapour-deposited layers, Philips Res. Rep. 22 (3) (1967) 267–288.

[41] R. Banerjee, E.A. Sperling, G.B. Thompson, H.L. Fraser, S. Bose, P. Ayyub, Lattice expansion in nanocrystalline niobium thin films, Appl. Phys. Lett. 82 (24) (Jun. 2003) 4250–4252, https://doi.org/10.1063/1.1582361.

[42] Y. Choi, S. Suresh, Size effects on the mechanical properties of thin polycrystalline metal films on substrates, Acta Mater. 50 (7) (2002) 1881–1893, Apr, https://doi.org/10.1016/S1359-6454(02)00046-0.

[43] M.A. Peck, Structural and Superconducting Properties of Sputter-Deposited Niobium Films for Applications in Rf Accelerating Cavities, Ph.D. Thesis, Technische Universität Wien, 1999.

[44] L.S. Yu, J.M.E. Harper, J.J. Cuomo, D.A. Smith, Control of thin film orientation by glancing angle ion bombardment during growth, J. Vac. Sci. Technol. A Vacuum, Surfaces, Film. 4 (3) (May 1986) 443–447, https://doi.org/10.1116/1.573902.

[45] M. Krishnan, et al., Energetic condensation growth of Nb thin films, Phys. Rev. Spec. Top. Accel. Beams 15 (3) (Mar. 2012), 032001, https://doi.org/10.1103/PhysRevSTAB.15.032001.

[46] F. Ying, R.W. Smith, D.J. Srolovitz, The mechanism of texture formation during film growth: the roles of preferential sputtering and shadowing, Appl. Phys. Lett. 69 (20) (1996) 3007–3009, Nov, https://doi.org/10.1063/1.116821.

[47] M. Krishnan, et al., Very high residual resistivity ratios of heteroepitaxial superconducting niobium films on MgO substrates, Supercond. Sci. Technol. 24 (11) (Nov. 2011), 115002, https://doi.org/10.1088/0953-2048/24/11/115002.

[48] X. Zhao, L. Phillips, C.E. Reece, K. Seo, M. Krishnan, E. Valderrama, Twin symmetry texture of energetically condensed niobium thin films on sapphire substrate (a -plane Al 2 O 3), J. Appl. Phys. 110 (3) (Aug. 2011), 033523, https://doi.org/10.1063/1.3611406.

[49] W. Wisniewski, S. Saager, A. Böbenroth, C. Rüssel, "Experimental evidence concerning the significant information depth of electron backscatter diffraction (EBSD),", Ultramicroscopy 173 (July 2016) (Feb. 2017) 1–9, https://doi.org/10.1016/j.ultramic.2016.11.004.

[50] S.G. Wang, E.K. Tian, C.W. Lung, Surface energy of arbitrary crystal plane of bcc and fcc metals, J. Phys. Chem. Solid. 61 (8) (Aug. 2000) 1295–1300, https://doi.org/10.1016/S0022-3697(99)00415-1.

[51] S.-B. Lee, J.E. LeDonne, S.C.V. Lim, I.J. Beyerlein, A.D. Rollett, The heterophase interface character distribution of physical vapor-deposited and accumulative roll-bonded Cu–Nb multilayer composites, Acta Mater. 60 (4) (2012) 1747–1761, Feb, https://doi.org/10.1016/j.actamat.2011.12.007.

[52] J. Bian, G. Wang, X. Feng, Atomistic calculations of surface energy of spherical copper surfaces, Acta Mech. Solida Sin. 25 (6) (Dec. 2012) 557–561, https://doi.org/10.1016/S0894-9166(12)60050-0.

[53] J.S. Carpenter, S.J. Zheng, R.F. Zhang, S.C. Vogel, I.J. Beyerlein, N.A. Mara, Thermal stability of Cu–Nb nanolamellar composites fabricated via accumulative roll bonding, Philos. Mag. A 93 (7) (Mar. 2013) 718–735, https://doi.org/10.1080/14786435.2012.731527.

[54] D.M. Gokhfeld, Analysis of superconductor magnetization hysteresis, J. Sib. Fed. Univ. Math. Phys. 11 (2) (May 2018) 219–221, https://doi.org/10.17516/1997-1397-2018-11-2-219-221.
[55] S.B. Roy, G.R. Myneni, V.C. Sahni, On the reliable determination of the magnetic field for first flux-line penetration in technical niobium material, Supercond. Sci. Technol. 21 (6) (Jun. 2008), 065002, https://doi.org/10.1088/0953-2048/21/6/065002.
[56] D.-X. Chen, C. Prados, E. Pardo, A. Sanchez, A. Hernando, Transverse demagnetizing factors of long rectangular bars: I. Analytical expressions for extreme values of susceptibility, J. Appl. Phys. 91 (8) (Apr. 2002) 5254–5259, https://doi.org/10.1063/1.1459745.